

# ABLATION OF CARBON-BASED MATERIALS: MULTISCALE ROUGHNESS MODELLING

Gerard L. Vignoles<sup>1</sup>, Jean Lachaud<sup>1</sup>, Yvan Aspa<sup>1,2</sup>, Jean-Marc Goyh  n  che<sup>1</sup>

<sup>1</sup> Laboratoire des Composites ThermoStructuraux (LCTS) - UMR 5801 Univ. Bordeaux 1-CNRS-SNECMA-CEA - 3, All  e La Bo  tie, Domaine Universitaire, Pessac, F33600 France

<sup>2</sup> Institut de M  canique des Fluides de Toulouse (IMFT) - UMR 5502 INPT-CNRS – 1, All  e du Professeur Camille Soula, Toulouse, F 31000 France

## ABSTRACT

Because of their unique ablative properties, many carbon-based heterogeneous materials are used as components for thermal protection of systems used at extreme temperatures, such as atmospheric re-entry shields and rocket nozzles. Among other issues, the design of such systems relies critically on the knowledge of surface roughness evolution. This paper gives a synthetic view of an approach of ablation, either by oxidation or by sublimation, which is started from the material point of view. First, the morphology is studied: various features and scales of roughness are presented, and a classification is proposed. Second, a modelling strategy is built. It is based on the competition between bulk and heterogeneous transfer, with possible reactivity contrasts between the material constituents. Numerical results at various scales are given. Some predicted morphologies are in correct agreement with the experimental observations. A parameter variation study shows that the morphological features are dictated by the reactivity contrast of the material components, and by diffusion/reaction competitions. This allows to identify physico-chemical parameters from the roughness geometry, as in an inverse method. The approach is validated quantitatively in the case of the oxidation of a 3D C/C composite.

## 1. INTRODUCTION

Among the well-known materials for atmospheric re-entry Thermal Protection Systems (TPS), carbon/carbon (C/C) and carbon/phenolic resin (C/R) composites, which are ablative, are of common use [1,2], because of their excellent compromise between thermal, thermo-chemical and mechanical properties [3]. The principle of thermal protection is that an appreciable amount of the received heat flux is converted into outwards mass flux through endothermic processes like sublimation and chemical etching, which induce surface recession [4]. Surface roughening then appears: this banal but uncontrolled phenomenon has several consequences of importance in the case of atmospheric re-entry. First, it increases the chemically active surface area of the wall; and second, it promotes the laminar-to-turbulent transition in the surrounding flow [5,6]. Both of these modifications to the physico-chemistry lead to an increase in heat transfer, resulting in

an acceleration of the surface recession [7]. The TPS thickness design has to take this rather strong effect into account.

Another spatial application for the same class of materials is the fabrication of rocket nozzle throats, divergents and inner parts. In this case, the dominant factor is the influence of roughness on the effective recession rate ; also, a rougher surface is more sensitive to mechanical erosion [8].

For both applications, if general phenomenological tendencies are predictable, the understanding of the interaction between the surrounding flow and the reactive, receding material has to be improved. In this work, an effort is done to enhance this comprehension through the observation, the study and the modelling of roughness evolution, focusing on the primary cause, which is heterogeneous transfer. This document brings an overview on the proposed approach and features three parts: First, a description and a classification of multi-scale surface roughness features appearing on carbon-based materials are proposed. The second part describes the physico-chemical models which are set up to explain the formation of the typical roughness patterns. The last part presents numerical and analytical, which are validated and discussed with respect to experimental observations.

## **2. ROUGHNESS OBSERVATION AND CLASSIFICATION**

The studied materials are:

(1) A 3D C/C composite, made from a 3D ex-PAN carbon fibre preform and a pitch-based carbon matrix. It is a heterogeneous multi-scale material. The “skeleton” of the composite consists in unidirectional bundles made of several thousands of fibres which are linked together by a pitch-based matrix (mesostructure). The bundles are fit together into a 3D orthogonal pattern repeated by translation on a cubic lattice. This

macro-structure leads to a network of parallelepipedic macro-pores (located near each node of the lattice), which are partially filled with a pitch-based carbon matrix.

(2) A pyrolysed C/phenolic resin composite, made of ex-cellulose fibres grouped in yarns, which are themselves woven in satin plies; the plies are stacked together and impregnated with phenolic resin. Under typical ablation conditions, the phenolic resin is not any more present as such, but has suffered pyrolysis and is transformed into a highly porous carbon with an approximate density of  $700 \text{ kg.m}^{-3}$ .

(3) Polycrystalline graphite samples, with grain size ranging between 3 and 5  $\mu\text{m}$ . The grains are bonded together by a less organised carbon obtained by carbonisation and graphitisation of pitch.

Unfortunately, it is quite difficult to recover samples from real flight experiments; however, as far as roughness is concerned, arc-jet ground tests are supposed to be representative of real flight conditions [9]. The samples have been submitted to arc-jet tests in stagnation point configuration. In this case, the material temperature is high enough (3000 K) to enable both oxidation and sublimation. Other tests have been performed in an atmospheric pressure oxidation reactor, with temperatures ranging from 773 to 973 K.

The sample surfaces have been observed by binocular magnifier (BM), optical microscope (OM), scanning electron microscopy (SEM), laser profilometry and X-ray Computed Micro-Tomography (CMT). The observed roughness features have been collected and classified as presented in Table 1. Several characteristic features are illustrated at figs. 1 to 6. The morphological patterns may be organised following two criteria: (1) the presence or absence of an underlying material heterogeneity, and (2) the characteristic length scale. Ablation features originated from the material heterogeneity will be called “structural roughness”; in the converse case we will refer to “physical roughness”.

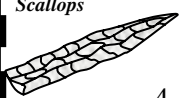
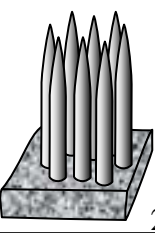
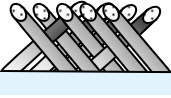
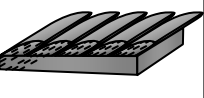




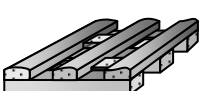

Structural roughness is easier to understand and describe. According to the characteristic length, it is possible to distinguish (the numbers refer to the corresponding cases in table 1):

(1) Epi-macrostructural roughness takes place on the lattice. It seems to result from the difference of reactivity between bundles and extra-bundle pitch-based matrix. Mechanical erosion sporadically occurs through the detachment of an extra-bundle matrix lump. The vertical bundles acquire a pyramidal shape. The section of bundles tangent to the surface is slightly undulating. Indeed, edges of bundles with an initially square section are emerging, creating crenulations in the underlying horizontal bundles, which are smoothed out to a wavy form by ablation, as visible on an OM micrograph presented on Fig. 1. Note that the present macro-scale has been termed “meso-scale” in past works on the same class of materials [10].

(2) Epimesostructural roughness develops at the top of emerging bundles. The surface of bundles perpendicular to the average material surface look like "needle clusters"; on the other hand, tangent bundles look like "needle layers". In the literature, many micrographs show similar roughness features on carbon-based composites during ablation by oxidation [11, 12] or both by oxidation and sublimation [13-15]. Fig. 2 suggests that, due to an important recession of the intra-bundle matrix, the fibres, which are less reactive, are partially stripped, become thinner, and acquire a needle shape.

(3) Epimicrostructural roughness appears on the microstructure. Fibre tips are faceted (Fig. 3). Some materials also show holes on the top of the fibres. In the same category, one finds the grain-related roughness of polycrystalline graphite, as illustrated at Fig. 5.

**Tab. 1.** Classification of roughness morphologies. The black boxes correspond to photographs of figs. 1-6. Thick,continuous line borders refer to structural roughness and dashed line borders refer to physical roughness.

Roughness Scale	MICRO-SCALE		MESO-SCALE		
Material scale	microstructure		mesostructure		composite
	fibre / grain	bundle	Weave pattern	Plies	REV
	micrometre		millimetre		centimetre
C/phen	 4	 2	 Inter-bundle	 Inter-plyes	 6
C/C	 3	 Intra-bundle	 Swivel	 1	
Polycr. Graphite		 Emerging grains. 5			

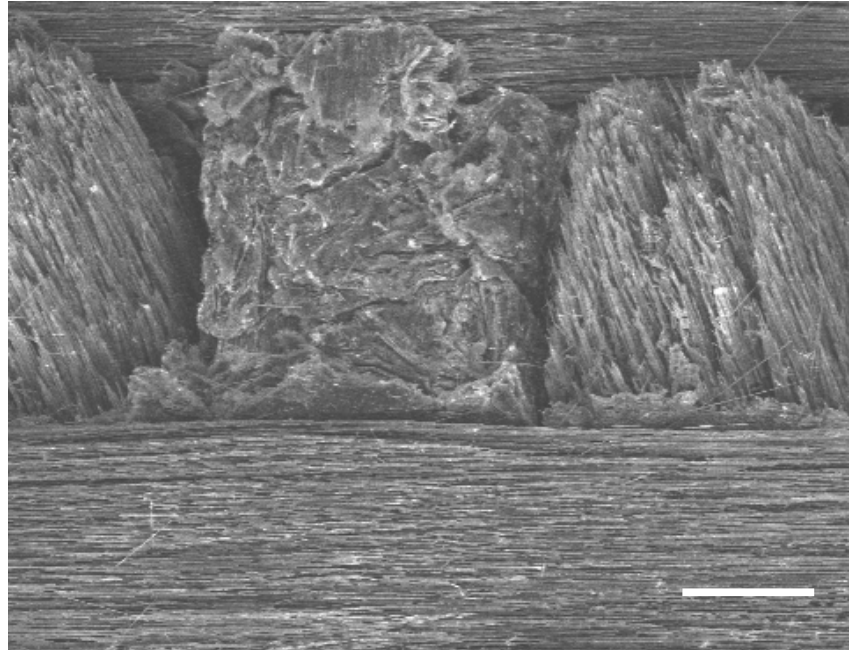


**Fig. 1.** Optical Micrograph of a 3D C/C composite after oxidation. The scale bar is approximately 0.3 mm long.

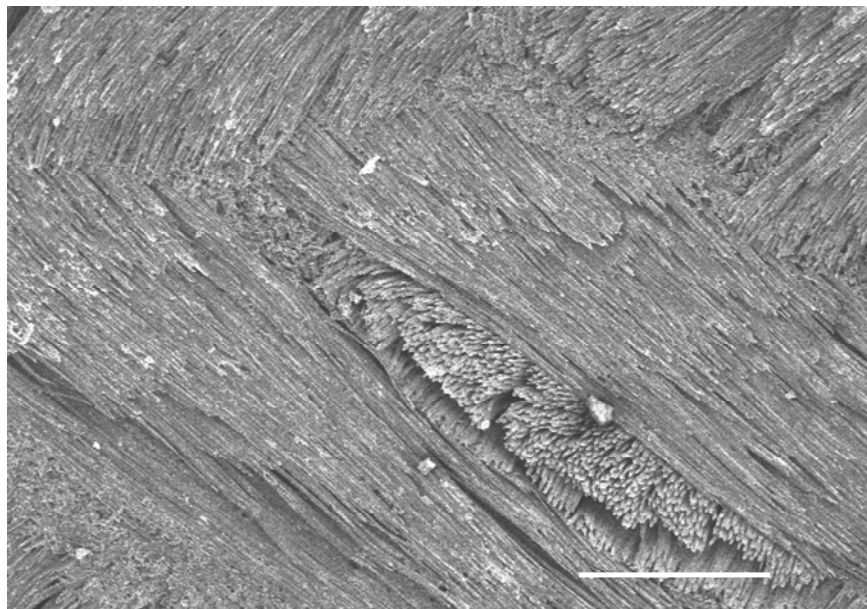


**Fig. 1bis.** Optical Micrograph of a 2D C/R composite after oxidation. The scale bar is approximately 0.3 mm long.

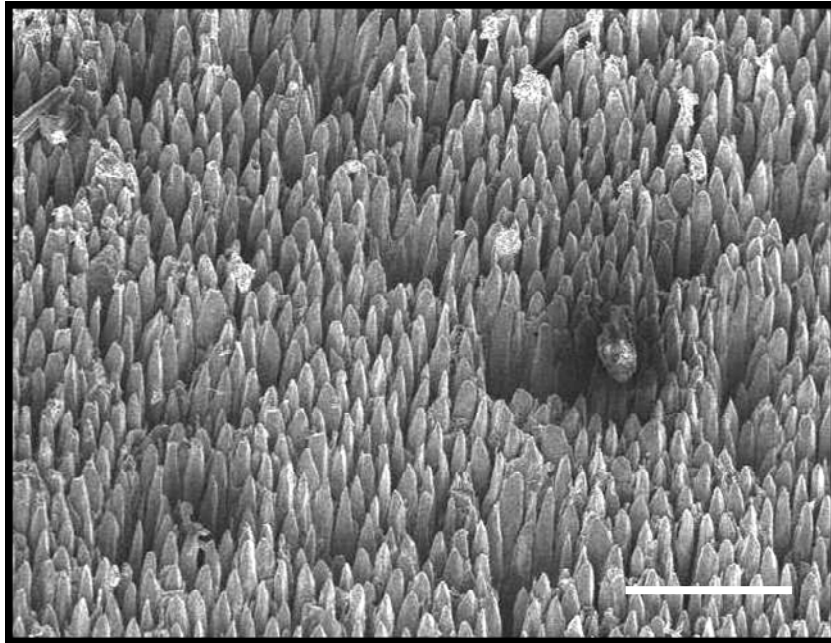


**Fig. 2.** SEM image of a “fibre forest”, in an emerging bundle of a 3D C/C composite. The scale bar is approximately 0.1 mm long.

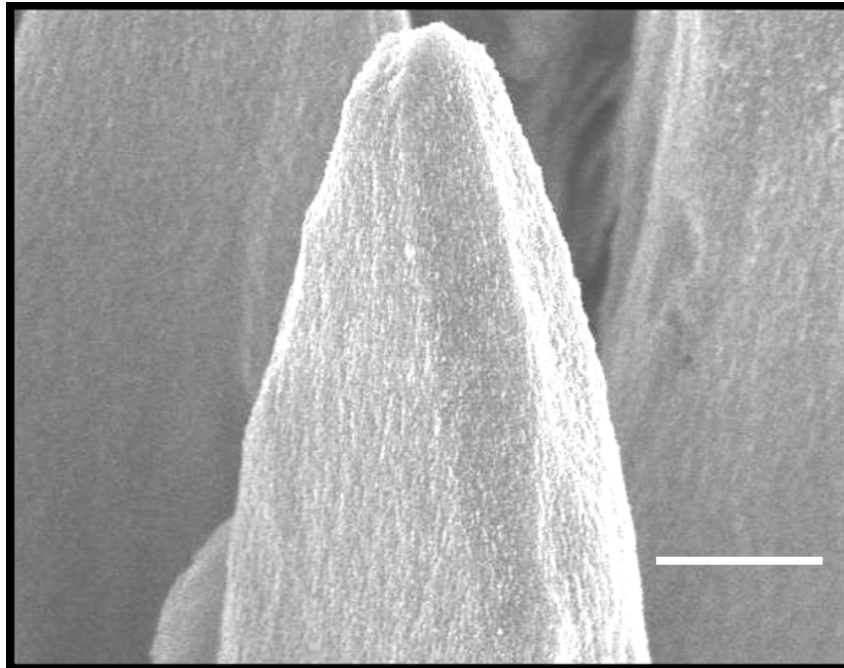


**Fig. 3.** SEM image of an ex-PAN fibre tip displaying facets (3D C/C composite). The scale bar is approximately 2  $\mu\text{m}$  long.



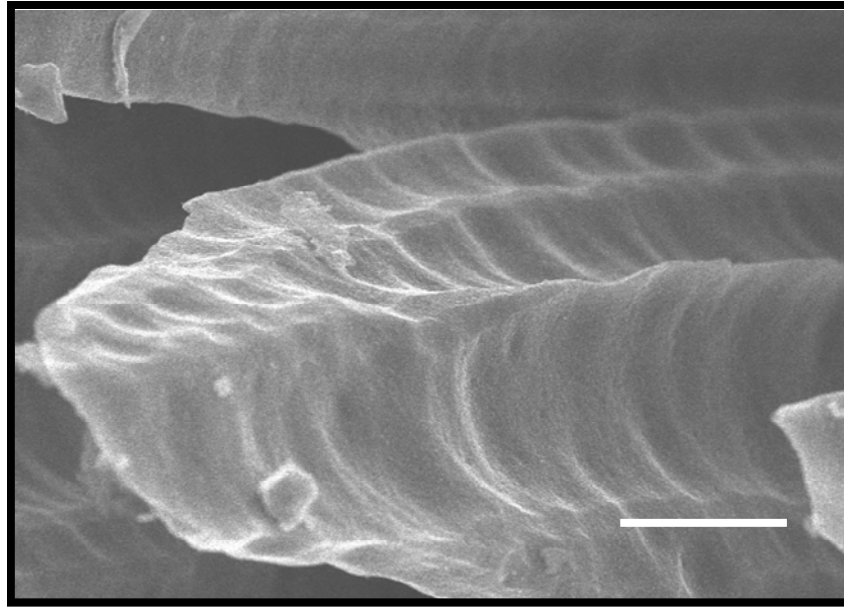


**Fig. 4.** SEM image of an ex-cellulose fibre tip displaying scallops (2D C/R composite). The scale bar is approximately 2  $\mu\text{m}$  long.

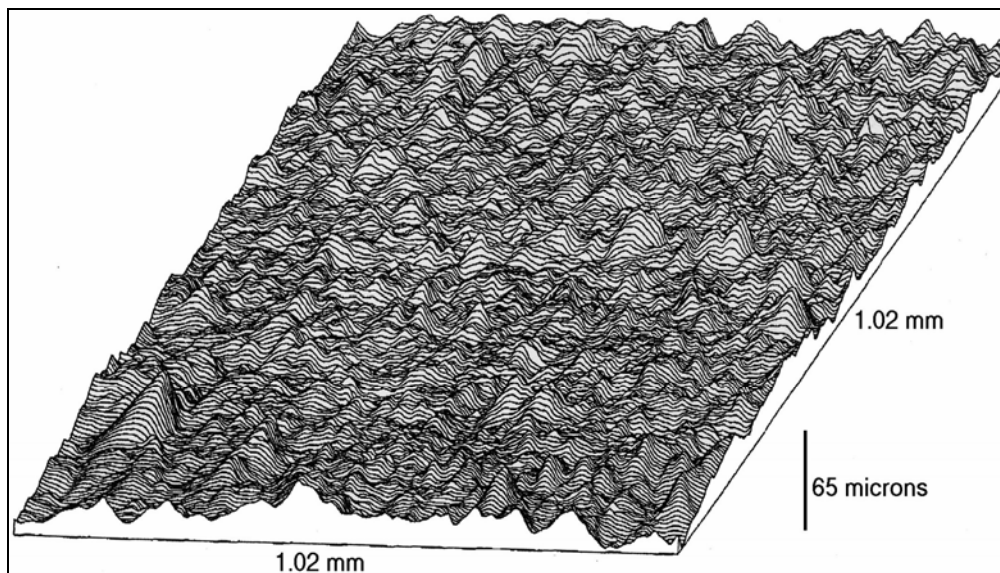


**Fig. 5.** Profilometric graph of a polycrystalline graphite sample ablated in laminar flow regime.

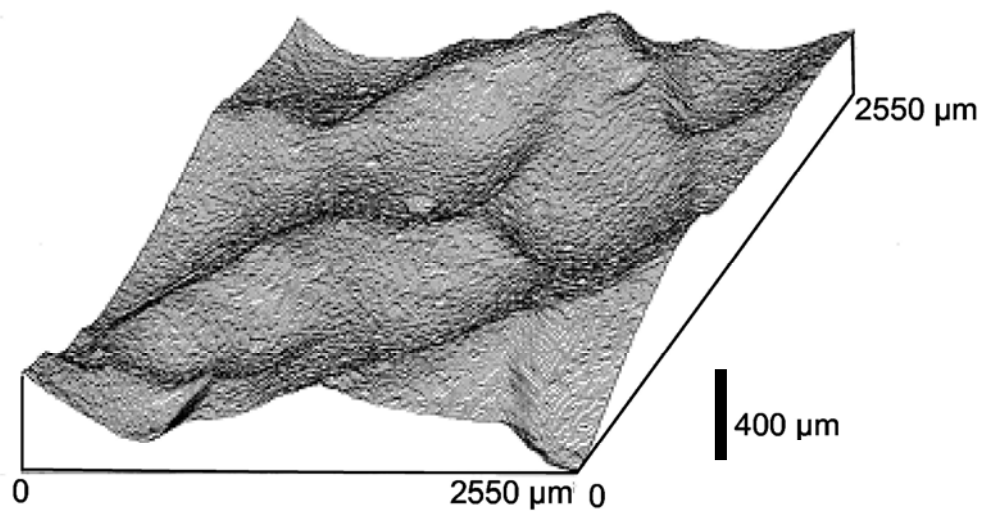


**Fig. 6.** Profilometric graph of a polycrystalline graphite sample ablated in turbulent flow regime.

The second kind of roughness features is identified on materials or material components which do not display evidence of local heterogeneity. It consists in “scallops” or “thumbprints”, which are similar to the “regmaglypts” observed on meteorites. These have been long ago described on materials which have suffered ablation tests [16,17] and are found again in the present observations, either on a naked fibre tip with mi-

crometer-long scallops (fig. 4) or on a polycrystalline graphite sample ablated in turbulent flow conditions, with millimetre-long features (fig. 6). The fact that two very distinct length scales exist on similar carbon-based materials will be addressed in the following. Evidently, physical roughness may only arise from transfer phenomena between the solid and the gas phases: this will be accounted for in the modelling strategy presented next.

### 3. MODELLING PRINCIPLES

From the morphological study presented above, it appears that the modelling of the roughness onset should feature four elements:

(i) **Surface recession**, under the action of oxidation or of sublimation. The surface recession velocity at any point depends on surface orientation, and on the rate of mass transfer. This is modelled by a Hamilton-Jacobi equation which describes the propagation of the surface. Taking  $S(x,y,z,t) = 0$  as an implicit representation of the surface, it writes :

$$\frac{\partial S}{\partial t} + \mathbf{v} \cdot \nabla S = 0 \quad (1)$$

The Hamiltonian  $H = \mathbf{v} \cdot \nabla S$  contains the actual normal surface recession velocity  $\mathbf{v}$ , which depends on the reaction rate  $R$  :

$$\mathbf{v} = \nu R \mathbf{n} \quad (2)$$

This rate depends *a priori* on surface temperature and of local concentration of reactant gas:

$$R = k_0 \exp(-E_a/\mathcal{R}T) \cdot C(z = h) \quad (3)$$

In the case of sublimation  $\mathbf{v}$  depends on the local partial pressure of sublimed species, compared to the equilibrium value, *e.g.* through a Knudsen-Langmuir relationship :

$$\mathbf{v} = \nu_s \cdot \alpha_0 \exp(-E_a/\mathcal{R}T) (2\pi\mathcal{R}TM)^{-1/2} [p_i(z = h) - p_i^{eq}(T(z = h))] \mathbf{n} \quad (4)$$

Equation (4) is very similar to equations (2-3); the problems of sublimation and oxidation are dynamically equivalent when (i) one replaces the concentration  $C$  by the under-saturation  $p_i - p_i^{\text{eq}}$  and (ii) one defines an equivalent reactivity  $k_0 = \alpha_0(2\pi\mathcal{R}TM)^{-1/2}$ .

Note that the normal to the surface is obtained from the gradient of the implicit function  $S(x,y,z,t)$  :

$$\mathbf{n} = \nabla S / \|\nabla S\| \quad (5)$$

When the surface does not contain any overhang, it is possible to write down the implicit function  $S$  as :

$$S(x,y,z,t) = z - h(x,y,t) \quad (6)$$

(ii) **The local gas concentration** is attained by solving a mass balance equation featuring transport in the bulk of the gas phase:

$$\frac{\partial C}{\partial t} + \nabla \cdot (\mathbf{v}_g C - D \nabla C) = 0 \quad (7)$$

and consumption or production by the surface :

$$-D \nabla C \cdot \mathbf{n} = -R \quad \text{for } S = 0, \text{ i.e. } z = h. \quad (8)$$

Gas-phase transport should feature diffusion (possibly multi-component), and convection. This last element requires knowledge of the gas phase velocity field  $\mathbf{v}_g$ , in possibly turbulent flow conditions, which may be extremely difficult to obtain in a realistic fashion.

(iii) Similarly, **the local surface temperature** is evaluated by a heat balance equation featuring transport in the solid gas phases:

$$\rho_g c_{pg} \left( \frac{\partial T}{\partial t} + \mathbf{v}_g \cdot \nabla T \right) + \nabla \cdot (-\lambda_g \nabla T) = 0 \quad (9)$$

$$\rho_s c_{ps} \frac{\partial T}{\partial t} + \nabla \cdot (-\lambda_s \nabla T) = 0 \quad (10)$$

, as well as interfacial heat consumption:

$$[-\lambda \nabla T \cdot \mathbf{n}]_{g \rightarrow s} = L_f R \quad (11)$$

(iv) When necessary, the **chemical reactivity** (*i.e.* the reaction constant  $k$  or the sticking probability  $\alpha$ ) will be a function of space, in order to account for the possible material heterogeneity.

A first model may be built using a set of restrictive assumptions:

- Isothermal conditions. This is suited to two kinds of situations: (1) isothermal oxidation tests; (2) micro-scale simulations where it appears that temperature differences across a characteristic roughness feature length are small enough to be neglected.
- Gas transport is restricted to the pure diffusion of a single species between the surface and a gas source (or sink) located at a large enough distance above the surface ; at this place, it is considered that convection ensures the constancy of gas concentration. The relation between source concentration and source-to-surface distance may be obtained through a boundary-layer analysis. The criterion for the choice of the source-to-surface distance is based on a perturbation analysis argument, which shows that it can be as small as a few times the transverse characteristic length of the roughness pattern.
- Surface gas transfer is first order. It can be shown that oxidation and sublimation follow the same formalism in these conditions [18].

The basic equations are:

$$\left\{ \begin{array}{l} \frac{\partial S}{\partial t} + \mathbf{v} \cdot \nabla S = 0 \\ \mathbf{v} = -\nu_s R \mathbf{n} \\ R = kC \quad \text{at} \quad S(x, y, z, t) = 0 \\ \nabla \cdot (-D \nabla C) = 0 \quad \text{at} \quad S(x, y, z, t) \geq 0 \\ -D \nabla C \cdot \mathbf{n} = -R \quad \text{at} \quad S(x, y, z, t) = 0 \end{array} \right. \quad (12)$$

Even though this model looks extremely restrictive, it has the merit of being easily tractable and of capturing the essentials of the bulk transport/interfacial transfer competition. Moreover, it will appear that most of the roughness set-up dynamics is governed

by the material itself, which will be correctly described by the model; on the other hand, it is absolutely not claimed to describe accurately the gas flow.

A second model may be easily built on the basis of the first one, by taking an analogy between heat and mass transfer; for this, it suffices to replace gas concentration by temperature. This will be adequate for large-scale modelling, where the gas diffusive boundary-layer thickness is very small with respect to the thermal boundary layer. The equations become then:

$$\left\{ \begin{array}{l} \frac{\partial S}{\partial t} + \mathbf{v} \cdot \nabla S = 0 \\ \mathbf{v} = -\nu_s R \mathbf{n} \\ R = k_0 C_0 \exp(-E_a / \mathcal{R}T) \quad \text{at} \quad S(x, y, z, t) = 0 \\ \nabla \cdot (-\lambda_g \nabla T) = 0 \quad \text{at} \quad S(x, y, z, t) \geq 0 \\ \nabla \cdot (-\lambda_s \nabla T) = 0 \quad \text{at} \quad S(x, y, z, t) \leq 0 \\ -[\lambda \nabla C \cdot \mathbf{n}]_{g \rightarrow s} = -L_r R \quad \text{at} \quad S(x, y, z, t) = 0 \end{array} \right. \quad (13)$$

Results from these two simple models (later on referred to as “Model 1” and “Model 2”) will be presented in the following part.

## 4. RESULTS

### 4. 1 - Physical Roughness (Scallops)

The simplest modelling case concerns Model 1 with a chemically homogeneous surface, and in steady state, that is, all surface points recede with a constant velocity  $V_{\text{eff}}$ . It becomes convenient to rewrite the systems in the coordinate frame moving with the surface. Then, an interesting simplification of the diffusion equation appears: one can consider that the concentration gradient is purely vertical. Considering that the concentration is constant and equal to  $C_0$  at a chosen altitude  $z = 0$ , one has:

$$C(z) = C_0 + D(z/h)(C(h)-C_0) \quad (14)$$

Equating the normal component of the diffusion flux to the reaction flux gives a full solution for  $C(z)$  ; then, substituting back into the Hamilton-Jacobi equation, one arrives finally at:

$$\frac{\partial h}{\partial t} = \frac{\nu_s C_0 k}{\frac{kh}{D} + \sqrt{1 + \left(\frac{\partial h}{\partial x}\right)^2 + \left(\frac{\partial h}{\partial y}\right)^2}} \quad (15)$$

A mathematical analysis of this equation [18] shows that there exist stable steady-state morphologies which are made of circle arcs (or sphere segments in 3D) or flat segments, connected together by symmetrical singular points (“cusps”), as shown at fig. 7.

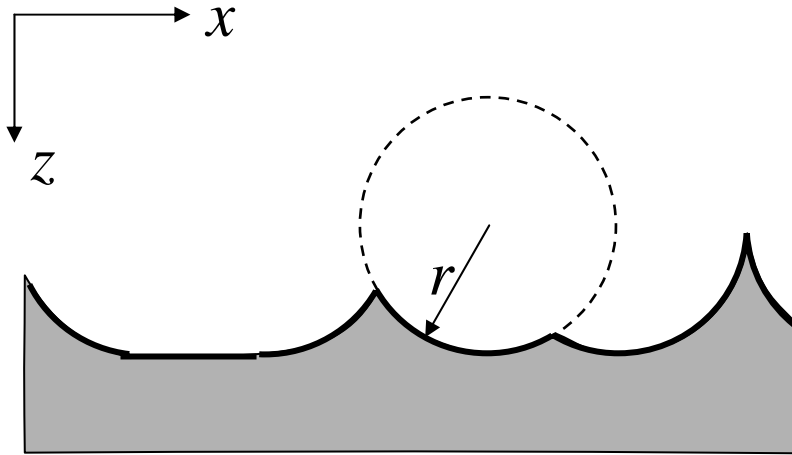


**Fig. 7 :** An admissible 2D steady-state solution for the diffusion-reaction-recession problem with homogeneous surface reactivity.

The curvature radius is simply  $r = D/k$ . Estimation of this quantity in the ablation case of fig. 4 (C/R fibre tip) yields a value of the order of 1  $\mu\text{m}$ , in agreement with the observed scallop curvature radius. Numerical simulations have confirmed the stability of the scalloped surfaces and shown that the transient times are short ( $\tau \approx 3 C_0 \nu_s k^2 / D$ ) [19]. The fact that scallops are obtained results from the growth of initial perturbations, which may have several origins, like local material heterogeneity, turbulence in the flow, or else.

Switching now to model 2, the diffusion coefficient is replaced by the gas thermal diffusivity  $a_g = \lambda_g / \rho_g c_{pg}$ , and the heterogeneous reaction constant has to be replaced by its temperature-related analogue, *i.e.* [20] :

$$k' = \frac{L_r}{C_{pg} T_0} \cdot \frac{E_a}{\mathcal{R} T_0} \cdot k(T_0) \quad (16)$$

where  $T_0$  is a reference surface temperature (for example, at scallop bottom).

This gives a new curvature radius expression:

$$r = \frac{a}{k'} = \frac{\mathcal{R} T_0}{E_a} \cdot \frac{\lambda_g T_0}{C_0 L_r k(T_0)}. \quad (17)$$

A numerical evaluation of this quantity [18,19] gives  $r \sim 3$  mm, matching well the situation depicted at Fig. 6.

As a conclusion, it is shown that physical roughness indeed results from a competition between bulk transfer (diffusion) and interfacial transfer (heterogeneous reaction). Surface elements having a higher altitude are closer to the source: this ensures that the total reactive flux, proportional to concentration, is larger. But if they are more inclined with respect to the horizontal plane, the projected flux is lowered; combining the contributions, they receive the same flux as elements which lie farther from the source but have a lower slope: this ensures the steadiness of the surface morphology. A perturbation analysis has confirmed that the scallops are unconditionally stable.

#### 4. 2 – Micro-scale roughness : needle clusters

The next case concerns Model 1 again, with a chemically heterogeneous surface: here, the model system is a moderately reactive fibre surrounded by a more reactive matrix ( $k_m > k_f$ ). Again, an analytical study, in an axi-symmetrical configuration, and with a



steady-state hypothesis, has allowed obtaining the equation of the ogival shape of the fibres. The peak-to-valley roughness is then given by the following formula [21]:

$$\frac{h_f}{r_f} = \frac{La}{r_f} \left( \sqrt{1 + 2\sqrt{A^2 - 1} \left( \frac{r_f}{La} \right)} - \left( \frac{r_f}{La} \right)^2 - 1 \right) \quad (18)$$

where the reactivity contrast parameter is:

$$A = \frac{k_m \nu_m}{k_f \nu_f} \quad (19)$$

Interestingly, one notes that the tip height is again dictated by a characteristic length  $La = D/k_m$  arising, as in the preceding section, from the competition between diffusive bulk transport and the matrix heterogeneous transfer. It is also practical to introduce a Sherwood number  $Sh_f = \underline{r_f La} = r_f k_m / D$ .

Numerical simulations of this problem have been performed independently with two solvers. The first is based on a finite difference scheme for diffusion, a VOF (Volume-Of-Fluid) model for surface recession, and a PLIC (PLanar Interface Construction) discretisation of the interface boundary [22,23]. The second one [24,25] is based on a Monte-Carlo-Random Walk (MC/RW) algorithm for gas diffusion, with a suited sticking probability law for surface reaction, and a Simplified Marching-Cube (SMC) discretisation of the interface [26]. Both solvers yield steady-state morphologies in very good agreement with the analytical formula [21,25,27].

Fig. 8 illustrates the numerically computed evolution of the tip shape for various values of the Sherwood number, fibre volume fraction, and reactivity contrast. The roughness tends to disappear when  $Sh_f$  becomes high, because bulk gas diffusion is the only limiting factor and the effect of reactivity contrast vanishes. Conversely, when heterogeneous reaction becomes limiting, the sharpest features are obtained. The curvature

radius of the ogival shape being equal to  $La$ , the fibre tip becomes conical for low values of  $Sh_f$ ; the value of the relative height  $h_f/r_f$  tends towards the contrast factor  $A$ . Finally, it can be pointed out that the relative tip height is not a function of the fibre volume fraction  $\phi_f$  (or relative radius  $\tilde{r}_f = \frac{r_f}{a/2} = \sqrt{\frac{\phi_f}{\pi}}$ ,  $a$  being the unit cell size).

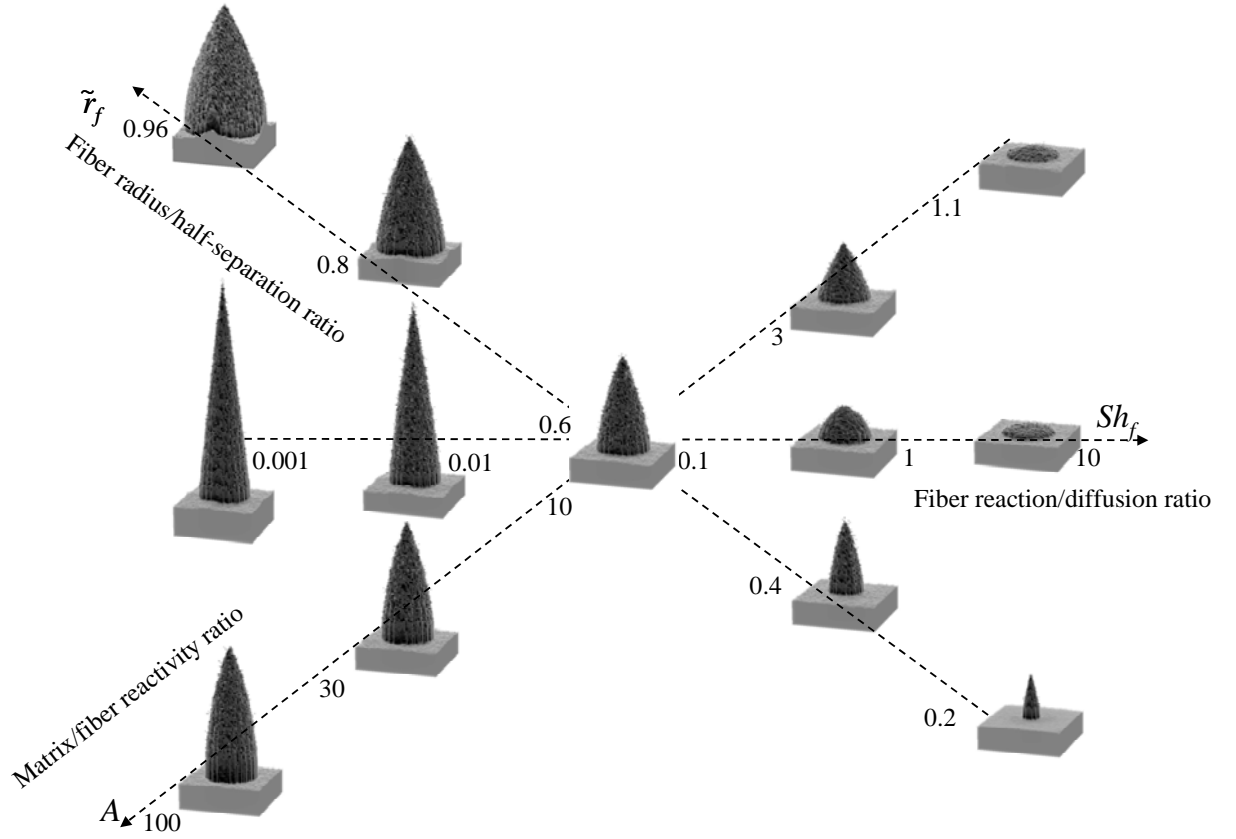


**Fig. 8 :** Influence of three dimensionless factors on the relative fiber tip height and curvature.

Glime and Cawley [28] had studied and modelled the oxidation of a C/SiC micro-composite. We have checked [21] : (i) that our approach was consistent with their analytical prevision (*i.e.*,  $h_f/r_f$  tends to  $A$  in the reaction-limited regime), (ii) that our numerical result fits well the analytical prevision, and (iii) that the numerical model of ref. [28] was giving some 10% error, possibly because of a non-optimal discretization of the interface.

Additionally, it appears that the transient time is the time needed for the fibre to be denuded. In the reaction-limited regime, one has the following estimate:

$$\tau \approx \frac{r_f \sqrt{A^2 - 1}}{k_f (\nu_f C_0) (A - 1)} \quad (20)$$

If the contrast is low, then this time may be very long. In the diffusion-limited regime, the characteristic transient time is roughly:

$$\tau \approx \frac{(\delta_c + h_f)^2}{(\nu_m C_0) D} \quad (21)$$

where  $\delta_c$  is the diffusive boundary layer thickness lying above the fibre tips. Note that in certain conditions, this may also be a rather long time.

The analytical and numerical studies also allow assessing the equivalent composite steady recession rate:

$$V_{eff} = (\nu_m C_0) \cdot k_m \cdot \frac{1}{1 + \frac{k_m (\delta_c + h_f)}{D}} \quad (22)$$

Eqs (21) and (22) show that the matrix reactivity is the most important control parameter, *i.e.* the weakest phase determines the composite behaviour. Using the combination of eqs (18) and (20), it is possible, as suggested by fig. 8, to perform a direct assessment of fibre and matrix reactivities from the study of the morphology and recession rate performed on unidirectional composites. This is illustrated in section 4.4.

#### 4.3 – Micro-scale roughness: grain-supported features

The case of polycrystalline graphite may be treated by Model 1, adding as an extra feature a dependence of the reactivity to orientation, which illustrates the anisotropy of

graphite. Indeed, graphene edge reactivity is known to be much larger than in the perpendicular direction. The following law for the orientation-dependent reactivity has been chosen:

$$k_{eff}(\theta) = \frac{k_{//}|\sin \theta| + k_{\perp}|\cos \theta|}{|\sin \theta| + |\cos \theta|} \quad (23)$$

Numerical simulation has been performed with the MC/RW-SMC algorithm, and yields typical morphologies as illustrated at fig. 9; comparing with fig. 5 shows that a very good qualitative agreement may be obtained. In this case, the grain-related peak-to-valley roughness is roughly 1/3 of the grain size [29].

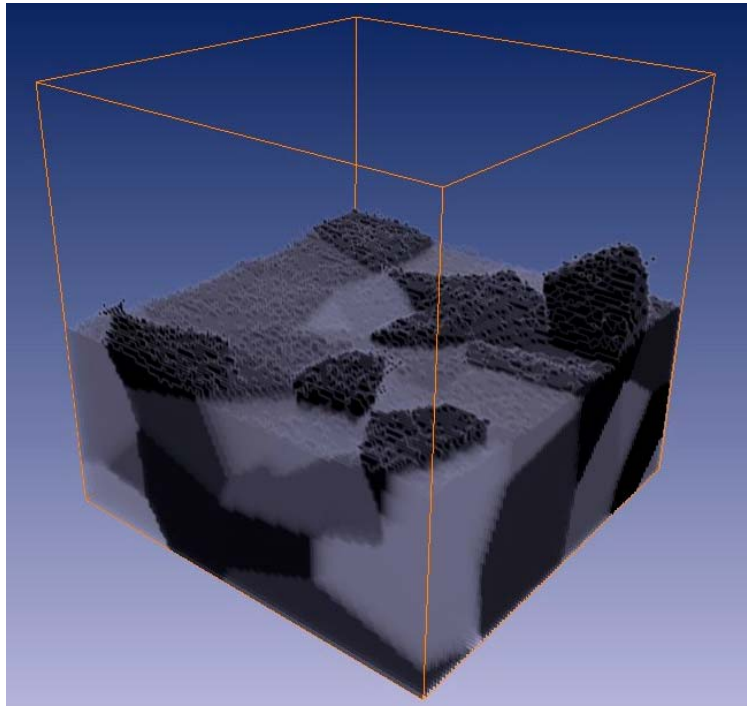


**Fig. 9 :** Example of roughness morphology simulation for polycrystalline graphite. Grains with graphene sheets lying parallel (resp. perpendicular) to the average surface are dark (resp; clear)

#### 4.4 Macro-scale features and mass loss

The last model case concerns large-scale simulation of epimacrostructural roughness. Here, Model 1 is used, and the model system is a 3D C/C composite with vertical and horizontal bundles of similar but anisotropic reactivity, and a more reactive inter-bundle matrix, under mild oxidation conditions : dry air,  $P = 1$  atm,  $T = 898$  K [27,30]. In this case, due to the large space scale, diffusion is nowhere limiting. However, since the intrinsic reactivity of the constituents is not known separately, a parameter variation study has been made in order to obtain the agreement, through a kind of inverse-problem analysis. First, the separate reactivities of the whole composite and of the lone fibres have been measured separately [30]. For this purpose, a tubular reactor in which the air flow and oxygen composition has been modelled by CFD analysis [27] in order to ensure a correct interpretation of the data in terms of actual intrinsic reactivities. Then, the analysis of the morphological parameters has allowed inferring the reactivity of the weakest phase, which is of utter importance in the present case since the weakest-link law rules. First, the fibre-scale parameters have been determined : the very sharp conical shape with  $h_f/r_f = 32$  ensures that one lies locally in the chemically-controlled regime, i.e.,  $Sh_f \ll 1$  ; accordingly, the contrast factor  $A$  is also equal to 32, which gives the weakest-phase reactivity as being 32 times the fibre's. The experimental determination of the fibre reactivity gives  $k_f = 1.2 \cdot 10^{-5} \text{ m.s}^{-1}$  ; so we infer that for the interphase  $k_i = 3.8 \cdot 10^{-4} \text{ m.s}^{-1}$ . From these values, the composite effective reactivity of a bundle has been determined in steady state: in the given conditions, since the weakest-link rule holds, its value is very close to the weakest-phase reactivity. It has been checked that the transient time at micro-scale (a few seconds) is very short with respect to the macro-scale transient time (close to one day). At larger scale, the image analysis of fig. 1 gave the following results: the bundle-scale Sherwood number  $Sh_b$  is also very low, and the contrast factor between bundles and the weakest phase (interphase around the bundles) is  $A = 8$ .

This gives weakest-phase and average reactivities equal to  $3.1 \cdot 10^{-3} \text{ m.s}^{-1}$ . The final result is within 3% of the experimental value ( $3.0 \cdot 10^{-3} \text{ m.s}^{-1}$ ).

With the obtained data, it has been possible to reproduce simultaneously and quantitatively the mass loss curve (fig. 10) and the ablated surface morphology (fig. 11). Though absolutely not evident from fig. 11, the model predicts that the steady state for the morphology evolution is not yet reached at the last data point ( $t = 960 \text{ min}$ ), a fact which is confirmed by direct observation of the sample after removal from the reactor. This illustrates the potential of the method in the extraction of material parameters from simple experimental data. When ablation is performed in non-isothermal conditions, identifications may be performed in exactly the same way, but making use of Model 2 instead of Model 1.

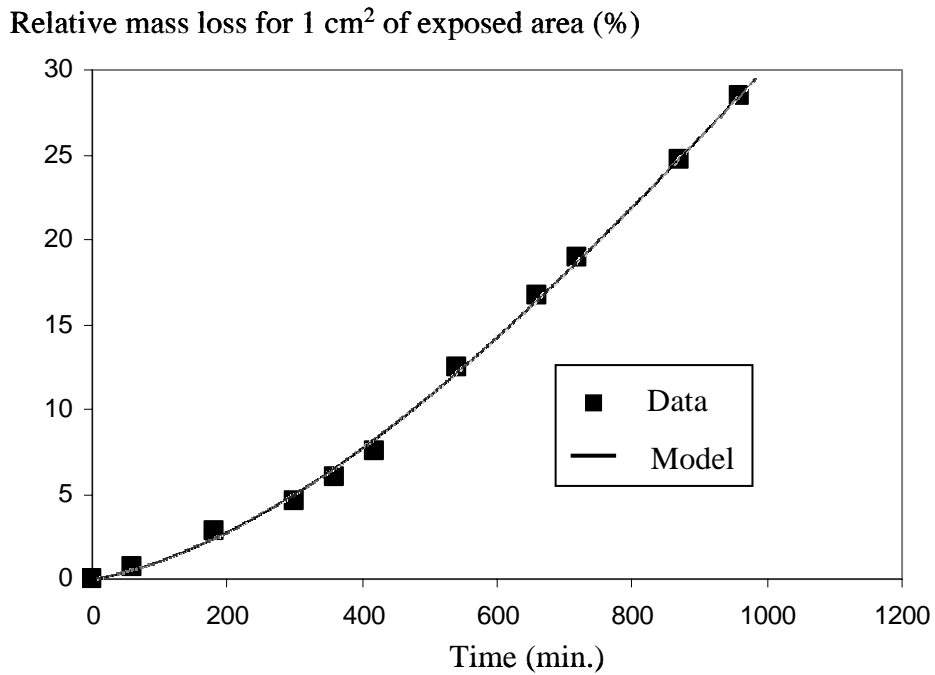


**Fig. 10 :** Experimental and modelled mass loss data for the oxidation of a 3D C/C composite in dry air at 898 K.

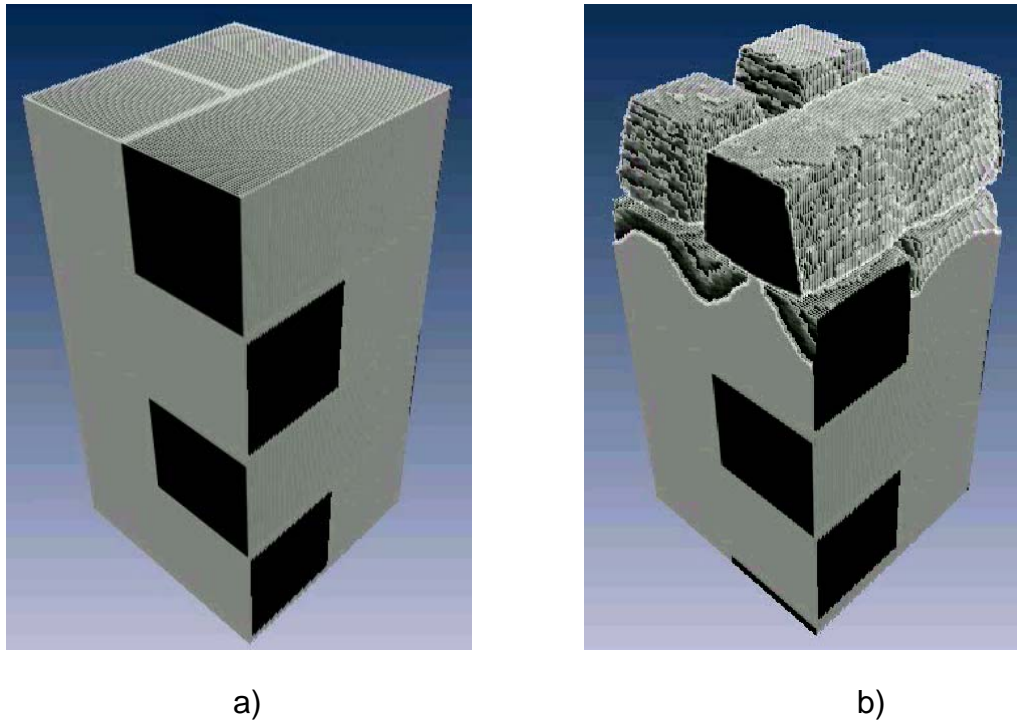


**Fig. 11** : 3D composite material macro scale ablation simulations : **a)** at  $t = 0$ , **b)** at  $t = 420$  min.

## 6. CONCLUSIONS AND OUTLOOK

This work shows that the large diversity of roughness feature morphologies and length scales may be explained and modelled with a rather simple approach based on the competition between bulk transfer and heterogeneous transfer, be it either of gas or of heat. The larger length scales are related to heat transfer, while the smallest are related to mass transfer. Reactivity (or heterogeneous transfer coefficient) differences between constituents are suited to explain structural roughness, while physical roughness (scallop) is explained by the bulk/interfacial transfer competition itself.

Many perspectives arise from these studies. First, more systematic experimental verifications have still to be performed in several situations, in order to confirm the predictive power of the approach. Second, exploitation in terms of guidelines for material optimization is at hand: it should be possible to use the presented tools to seek composites

with less pronounced roughness and /or equivalent reactivities. Third, the modelling tools have to be improved in several points: simultaneous resolution of heat & mass transfer, coupling with flow computations for the inclusion of convection, multicomponent diffusion, etc .... These will be the aim of future works.

## **ACKNOWLEDGEMENTS**

The authors acknowledge Snecma Propulsion Solide for a PhD grant to Y. A., and Commissariat à l'Energie Atomique for a grant to J. L.



## LIST OF SYMBOLS

Symbol	Meaning	Unit
$a$	Thermal diffusivity	$\text{m}^2.\text{s}^{-1}$
$A$	Reactivity contrast	-
$c_p, C_p$	Mass and molar heat capacities	$\text{J.kg}^{-1}.\text{K}^{-1}$ ; $\text{J.mol}^{-1}.\text{K}^{-1}$
$C$	Concentration	$\text{mol.m}^{-3}$
$D$	Diffusion coefficient	$\text{m}^2.\text{s}^{-1}$
$E_a$	Activation energy	$\text{J.mol}^{-1}$
$h_f$	Fibre height	m
$k$	Heterogeneous reaction constant	$\text{m.s}^{-1}$
$k'$	Temperature-related analogue of $k$ (eq. 16)	$\text{m.s}^{-1}$
$La$	Characteristic length	m
$L_r$	Molar heat of ablation	$\text{J.mol}^{-1}$
$M$	Molar mass	$\text{kg.mol}^{-1}$
$\mathbf{n}$	Exterior normal to the surface	-
$p_i$	Partial pressure of gas species $i$	Pa
$r$	Radius	m
$\mathcal{R}$	Perfect gas constant	$\text{J.mol}^{-1}.\text{K}^{-1}$
$R$	Surface reaction rate	$\text{mol.m}^{-2}.\text{s}^{-1}$
$S$	Surface function	-
$T$	Temperature	K
$\mathbf{v}$	Surface local velocity vector	$\text{m.s}^{-1}$
$V_{eff}$	Effective recession velocity	$\text{m.s}^{-1}$
$\alpha$	Sticking coefficient	-
$\delta_c$	Boundary layer thickness for mass transfer	m
$\theta$	Angle between normal and intrinsic graphene orientation	rad
$\lambda$	Heat conductivity	$\text{W.m}^{-1}.\text{K}^{-1}$
$\rho$	Density	$\text{kg.m}^{-3}$
$\tau$	Characteristic time	s
$\nu$	Molar volume	$\text{m}^3.\text{mol}^{-1}$
$\square_f$	(Subscript) Relative to fibre	
$\square_g$	(Subscript) Relative to gas	

$\square_m$	(Subscript) Relative to matrix (or weak phase)	
$\square_s$	(Subscript) Relative to solid	
$\square_0$	(Subscript) Relative to reference	

## References

1. **Manocha, L. M.** and **Fitzer, E.**, "Carbon reinforcement and C/C composites". Springer, Berlin (1998).
2. **Duffa, G.**, "Ablation". CEA, Le Barp, France ISBN 2-7272-0207-5 (1996)
3. **Savage, G.**, "Carbon/Carbon Composites". Chapman & Hall, London (1993).
4. **Couzi, J., de Winne, J.** and **Leroy, B.**, "Improvements in ablation predictions for reentry vehicle nosetip". In *Proc. 3rd Eur. Symp. on Aerothermodynamics for Space Vehicles*, ESA, Noordwijk, The Netherlands (1998), pp. 493-499.
5. **Jackson, M. D.**, "Roughness induced transition on blunt axisymmetric bodies", Interim Report SAMSO-TR-74-86 of Passive Nosetip Technology (PANT) Program n°15 (1974).
6. **Reda, D. C.**, "Correlation of nosetip boundary-layer transition data measured in ballistic-range experiments", Sandia Report SAND 79-0649 (1979).
7. **Batt, R. G.** and **Legner, H. H.**, "A review of roughness-induced nosetip transition", *AIAA Papers* **21**(1983), 7-22.
8. **Borie, V., Maisonneuve, Y., Lambert, D.** and **Lengellé, G.**, "Ablation des matériaux de tuyères de propulseurs à propergol solide". Technical Report N°13, ONERA, France (1990).
9. **Wool, M. R.**, "Summary of experimental and analytical results", Interim Report SAMSO-TR-74-86 of Passive Nosetip Technology (PANT) Program n°10 (1975).
10. **Dumont J.-P., Ladevèze P., Poss M., and Remond Y.**, "Damage mechanics for 3D composites". *Composite Structures* **8** (1987) 119-141.
11. **Cho, D., Lee, J. Y., and Yoon, B. I.**, "Microscopic observations of the ablation behaviours of carbon fibre/phenolic composites". *J. Mater. Sci.* **12** (1993) 1894-1896.
12. **Duvivier, E.**, "Cinétique d'oxydation d'un composite carbone/carbone et influence sur le comportement mécanique". PhD thesis n° 1692, University Bordeaux 1, France (1997).
13. **Cho, D.** and **Yoon, B. I.**, "Microstructural interpretation of the effect of various matrices on the ablation properties of carbon-fiber-reinforced composites". *Compos. Sci. and Technol.*, **61** (2001) 271-280.
14. **Han, J. C., He, X. D.** and **Du, S. Y.**, "Oxidation and ablation of 3D carbon-carbon composite at up to 3000 °C". *Carbon* **33** (1995) 473-478.
15. **Lee, Y.-J.** and **Joo, H.-J.**, "Investigation on ablation behavior of CFRC composites prepared at different pressures". *Composites: Part A* **35** (2004) 1285-1290.
16. **Larson, H. K.** and **Mateer, G. G.**, "Cross-hatching - A coupling of gas dynamics with the ablation process", *AIAA Paper* **68**-670 (1968).
17. **Williams, E. P.**, "Experimental Studies of Ablation Surface Patterns and Resulting Roll Torques", *AIAA J.* **9** (1971) 1315-1321.
18. **Duffa, G., Vignoles, G. L., Goyhénèche, J.-M.** and **Aspa, Y.**, "Ablation of carbon-based materials : investigation of roughness set-up from heterogeneous reactions". *Int. J. Heat and Mass Transfer*, **48** (2005) 3387-3401.
19. **Vignoles, G. L., Goyhénèche, J.-M., Duffa, G., N'guyen-Bui, T.-H., Velghe, A., Dubroca, B.** and **Aspa, Y.**, "Scalloped morphologies of ablated materials", *Ceram. Eng. Sci. Proc.* **26** (2005) 245-252.
20. **Vignoles, G. L., Lachaud, J.** and **Aspa, Y.**, "Roughness evolution in ablation of carbon-based materials : multi-scale modelling and material analysis", In *Proc. 5th Eur. Workshop on Thermal Protection Systems and Hot Structures*, ESA, Noordwijk, The Netherlands, *ESA Conf. Procs. SP-631* (2006).
21. **Lachaud, J., Aspa, Y., and Vignoles, G. L.**, "Analytical modeling of the steady state ablation of a 3D C/C composite", *Int. J. of Heat and Mass Transfer*, **51**(2008), 2614-2627.
22. **Aspa, Y., Quintard, M., Plazanet, F., Descamps, C.** and **Vignoles, G. L.**, "Ablation of Carbon/Carbon Composites : Direct Numerical Simulation and Effective Behavior", *Ceram. Eng. Sci. Proc.* **26** (2005) 99-106.
23. **Aspa, Y., Lachaud, J., Vignoles, G. L.** and **Quintard, M.**, "Simulation of C/C composites ablation using a VOF method with moving reactive interface", *ECCM12 proceedings*, J. Lamon and A. Torres-Marques eds., ESCM (2006), no. 385.

24. **Lachaud, J., Vignoles, G. L., Goyh  n  che, J.-M. and Eph  rre, J.-F.**, “Ablation in carbon/carbon composites : microscopic observations and 3D numerical simulation of surface roughness evolution”, *Ceram. Trans.* **191** (2005), 149-160.
25. **Lachaud, J., Vignoles, G. L.**, « A Brownian Motion simulation technique to simulate gasification and its application to ablation », *Comput. Mater. Sci.*, to appear (2008)
26. **Vignoles, G. L.**, “Modelling Binary, Knudsen, and Transition Regime Diffusion Inside Complex Porous Media”, *J. de Physique IV* **5** (1995) C5-159 – C5-166.
27. **Lachaud, J., Aspa, Y., Vignoles, G. L. and Bourget, G.**, “Experimental characterization and 3D modelling of carbon/carbon composites oxidation : role of the interface”, *ECCM12 proceedings*, J. Lamon and A. Torres-Marques eds., ESCM (2006), ref. 097.
28. **Glime, W. H., and Cawley, J. D.**, “Oxidation of carbon fibers and films in ceramic matrix composites: A weak link process”, *Carbon* **33** (1995) 1053-1060.
29. **Lachaud, J., Aspa, Y., Vignoles, G. L. and Goyh  n  che, J.-M.**, “3D modeling of thermochemical ablation in carbon-based materials: effect of anisotropy on surface roughness onset”, In *Proc.10th ESA International Symposium on Materials in a Space Environment (ISMSE 2006)*, ESA, Noordwijk, The Netherlands *ESA Conf. Procs.* **SP-616** (2006).
30. **Lachaud, J., Bertrand, N., Vignoles, G. L., Bourget, G., Rebillat, F. and Weisbecker, P.**, “Intrinsic oxidation reactivities of C/C composites and of their components: a theoretical/experimental approach », *Carbon* **45** (2007), 2768-2776